Supplementary Material to

A late Miocene dust shower from the break-up of an asteroid in the main belt

Samples

Carbonate sediments were studied from two deep sea cores. A suite of samples spanning from the middle Eocene to ~3 Ma was obtained from Hole 757B in the central Indian Ocean, 17°01.458'S, 88°10.899'E, on the Ninety East Ridge. This hole was cored on Leg 121 of the Ocean Drilling Program and has been described in detail[1]. Over the studied time interval this site is thought to have subsided from a middle Eocene depth of ~1500 m to its present depth of 1650 m. Sediments from this site are extremely pure carbonate oozes (usually >95% $CaCO_3$) that have accumulated at a fairly slow average rate of 0.35 cm/kyr. The purpose of this suite was to identify any intervals worthy of more detailed study at sites with faster accumulation rates and hence higher temporal resolution. ~140 samples were analyzed at about 1 meter intervals from ~18 to ~ 135 mbsf, except in two areas of interest, in the Late Eocene and the Late Miocene, where sampling density was higher.

Based on elevated extraterrestrial ^{3}He concentrations in the late Miocene an additional suite of samples was obtained from amongst the best studied cores spanning this interval, from Hole 926B. This hole was drilled on the Ceara Rise, western equatorial Atlantic (3°43.148'N, 42°54.507'W, 3600 m water depth) on Leg 154 of the Ocean Drilling Program[2]. The Late Miocene interval is a clayey carbonate ooze (~65% $CaCO_3$) with a mean accumulation rate of ~1.7 cm/kyr. 73 samples were analyzed in the interval between 159 and 224 mbsf. The spacing of these samples is ~ 1.5 meters away from the ^{3}He peak to as close as a few cm at the peak.

Methods

Samples were analyzed for helium isotopes following removal of $CaCO_3$ using standard procedures at Caltech[3]. In all cases ^{3}He and ^{4}He blank levels were sufficiently low compared to sample signals that blank corrections were not required. Many samples were analyzed in duplicate to detect and eliminate anomalously high ^{3}He values arising from occasional over-sampling of large IDP grains[4]. When preparing the final ^{3}He and ^{3}He/^{4}He data set the following procedure was adopted for incorporating replicated analyses. If the duplicates agreed to within a factor of three, the average was used. If the difference exceeded a factor of three, the higher value was excluded. This led to exclusion of about 6% of the ^{3}He measurements. For ^{4}He and non-carbonate fraction data the replicates were simply averaged.

Age Models

Site 757

The age model for site 757 comes primarily from shipboard biostratigraphy. Event locations are from the shipboard report[1] with updated datum ages from Backman and Raffi[5]. To facilitate comparison with previous wok at the Massignano GSSP,

biostratigraphic event ages for the Eocene were adopted[6]. Additional ages based on Sr isotope ratios[7] provide greater resolution through the Oligocene portion of the core. There is no magnetostratigraphy available for this core. Ages were assigned to samples by interpolating between tie points in the age model. Linear sedimentation rates (LSRs) were calculated between each tie point (Figure S1). Mass accumulation rates were computed by multiplying linear sedimentation rates interpolated for each depth by the dry bulk density from the Shipboard Report[1] interpolated for that same depth. Martin and Scher[7] have suggested the possibility of a hiatus in the lower Miocene portion of this core. Our observations provide no evidence for the existence of a hiatus, but the interval between about 20 and 15 Ma must be interpreted with caution. This is substantially lower in the core than the Late Miocene ^{3}He peak (Figure S1).

Site 926

At Site 757 the onset of the ^{3}He peak coincides with the first occurrence of the index fossil *D. quinqueramus* (a morphotype of *D. bergrenni*), which has an astronomically calibrated age of 8.2 Myr (ref 5). To test that the ^{3}He peak is global, we used this tie point to select coeval sediments from Site 926, located more than 10,000 km from Site 757. Detailed biostratigraphy[5] and orbitally-tuned cyclostratigraphy based on magnetic susceptibility[8] have been undertaken on the Miocene portion of Site 926 and provide a high resolution age model for this work. While both biostratigraphy and orbital tuning could be used to determine linear sedimentation rates, the orbitally-tuned model yields a seemingly unrealistic amount of high frequency variability in LSR (Figure S1). Instead the lower resolution biostratigraphic model was used to interpolate LSRs for each sample. These values were multiplied by a constant dry bulk density appropriate for this depth interval at Site 926 (1.28 g/cm^3 (ref 2) to obtain mass accumulation rates.

Results.

Measurements from the two sites are tabulated below and plotted against depth in supplementary Figures S2 and S3.

Leg 121
Hole 757B

Sample			MBSF Depth	Age	3He	3He/4He	ET3He flux	Non-Carbonate
Core	Segment	cm	Meters	(Ma)	(fmol/g)	(x10-6)	fmol/cm2/kyr	Fraction
3H	3	130	18.3	3.0571	0.0121	6.8222	0.0055	0.0131
3H	4	81	19.31	3.1971	0.0086	6.7438	0.0043	0.0112
3H	5	31	20.31	3.3357	0.0178	12.1688	0.0097	0.0116
3H	6	11	21.61	3.5158				0.0114
3H	6	111	22.61	3.6544	0.0155	7.9254	0.0099	0.0107
3H	7	61	23.61	3.7821	0.0273	16.6124	0.0184	0.0099
4H	1	95	24.55	3.8794	0.0122	7.1806	0.0084	0.0121
4H	2	45	25.55	3.9829	0.0156	9.1882	0.0111	0.0113
4H	2	144	26.54	4.0854	0.0288	19.6784	0.0210	0.0110

4H	3	94	27.54	4.1889	0.0143	8.3510	0.0107	0.0115
4H	4	44	28.54	4.2924	0.0232	16.1084	0.0178	0.0110
4H	4	144	29.54	4.3959	0.0151	11.6074	0.0119	0.0105
4H	5	94	30.54	4.4994	0.0142	14.8428	0.0115	0.0084
4H	6	44	31.54	4.6030	0.0125	11.5178	0.0103	0.0059
5H	1	88	34.08	4.8659	0.0218	24.7842	0.0191	0.0086
5H	2	38	35.08	4.9694	0.0200	23.6460	0.0180	0.0079
5H	2	138	36.08	5.1261	0.0105	14.4228	0.0096	0.0086
5H	3	87	37.07	5.1754	0.0075	11.7768	0.0070	0.0141
5H	4	37	38.07	5.2789	0.0186	17.2046	0.0179	0.0095
5H	4	138	39.08	5.3850	0.0154	24.3922	0.0151	0.0065
5H	5	88	40.08	5.5002	0.0137	21.8988	0.0131	0.0065
5H	6	38	41.08	5.6154	0.0151	20.8712	0.0142	0.0076
6H	2	20.5	44.505	6.0467	0.0123	17.7996	0.0108	0.0079
6H	2	120.5	45.505	6.2003	0.0112	11.2028	0.0097	0.0121
6H	3	67.5	46.475	6.3493	0.0119	15.9292	0.0101	0.0075
6H	4	20.5	47.505	6.5075	0.0095	12.2696	0.0079	0.0080
6H	4	122.5	48.525	6.6642	0.0152	19.4110	0.0122	0.0077
6H	5	69.5	49.495	6.8132	0.0075	11.4268	0.0059	0.0071
6H	6	20.5	50.505	6.9683	0.0106	12.1016	0.0081	0.0077
6H	6	118.5	51.485	7.1189	0.0100	14.2268	0.0075	0.0065
7H	1	36.5	52.865	7.3309	0.0105	24.2130	0.0075	0.0051
7H	1	140.5	53.905	7.4504	0.0143	21.9856	0.0106	0.0100
7H	2	90.5	54.905	7.5426	0.0089	14.1456	0.0071	0.0060
7H	3	140.5	56.905	7.7271	0.0158	21.6538	0.0143	0.0071
7H	4	90.5	57.905	7.8193	0.0176	24.3012	0.0169	0.0084
7H	5	40.5	58.905	7.9115	0.0204	36.3188	0.0208	0.0057
7H	5	140.5	59.905	8.0038	0.0219	28.8260	0.0235	0.0067
8H	1	5.5	62.255	8.2205	0.0378	54.9003	0.0456	0.0072
8H	1	100.5	63.205	8.3311	0.0043	6.1642	0.0052	0.0086
8H	2	50.5	64.205	8.4985	0.0036	4.4254	0.0042	0.0078
8H	2	75.5	64.455	8.5404	0.0073	14.8820	0.0084	0.0040
8H	2	100.5	64.705	8.5822	0.0033	10.1094	0.0037	0.0030
8H	3	3.5	65.235	8.6710	0.0066	11.5556	0.0072	0.0078
8H	3	20.5	65.405	8.6994	0.0063	6.4988	0.0068	0.0030
8H	3	40.5	65.605	8.7329	0.0056	9.8028	0.0061	0.0047
8H	3	60.5	65.805	8.7664	0.0031	8.1298	0.0033	0.0030
8H	3	80.5	66.005	8.7999	0.0107	22.6618	0.0113	0.0040
8H	3	100.5	66.205	8.4384	0.0040	5.8240	0.0041	0.0066
8H	3	145.5	66.655	8.9087	0.0024	4.6900	0.0024	0.0040
8H	4	50.5	67.205	9.0008	0.0076	13.0088	0.0074	0.0105
8H	5	10.5	68.305	9.1850	0.0085	12.7960	0.0077	0.0083
8H	5	110.5	69.305	9.3525	0.0116	20.6864	0.0099	0.0078
8H	6	60.5	70.305	9.5199	0.0063	11.5710	0.0050	0.0047
8H	7	10.5	71.305	9.6873	0.0075	13.6626	0.0054	0.0077
9H	1	78.5	72.585	10.0637	0.0062	11.9014	0.0042	0.0073
9H	2	38.5	73.685	10.4121	0.0046	9.0454	0.0030	0.0075
9H	2	140.5	74.705	10.2137	0.0229	28.7238	0.0145	0.0094
9H	3	91.5	75.715	11.0550	0.0094	12.0274	0.0057	0.0100
9H	4	38.5	76.685	11.3623	0.0110	17.4202	0.0064	0.0095

9H	5	120.5	79.005	12.0971	0.0182	33.7386	0.0095	0.0086
9H	6	68.5	79.985	12.4075	0.0131	23.4304	0.0065	0.0083
9H	7	20.5	81.005	12.7306	0.0291	50.8984	0.0137	0.0111
10H	2	29.5	83.295	13.4559	0.0332	34.6430	0.0136	0.0121
10H	2	129.5	84.295	13.9781	0.0233	22.6128	0.0090	0.0106
10H	3	82.5	85.325	14.6927	0.0246	21.0350	0.0088	0.0114
10H	4	129.5	87.295	16.0594	0.0492	48.7564	0.0153	0.0100
10H	5	80.5	88.305	16.7602	0.0324	13.5016	0.0093	0.0177
10H	6	28.5	89.285	17.4401	0.0194	11.9644	0.0050	0.0122
11H	1	28.5	91.485	18.9664	0.0906	41.4778	0.0185	0.0221
11H	1	128.5	92.485	19.5190	0.0489	16.2078	0.0114	0.0229
11H	2	80.5	93.505	19.8429	0.0317	16.1056	0.0112	0.0246
11H	3	30.5	94.505	20.1818	0.0398	25.4681	0.0155	0.0209
11H	3	130.5	95.505	20.7375	0.0268	18.7166	0.0073	0.0205
11H	4	82.5	96.525	21.5121	0.0334	17.3628	0.0051	0.0217
11H	5	30.5	97.505	22.2341	0.0414	20.3840	0.0076	0.0221
11H	5	132.5	98.525	22.9562	0.0637	37.1187	0.0121	0.0176
11H	6	82.5	99.525	23.6082	0.1058	33.3998	0.0214	0.0341
11H	7	30.5	100.505	24.2651	0.0684	17.1780	0.0141	0.0293
12H	1	85.5	101.655	24.9123	0.0298	24.8178	0.0067	0.0144
12H	2	34.5	102.645	25.4258	0.0651	40.4124	0.0171	0.0240
12H	2	135.5	103.655	25.9675	0.0244	11.3006	0.0065	0.0161
12H	3	85.5	104.655	26.4453	0.0259	19.2374	0.0075	0.0186
12H	4	15.5	105.455	26.8120	0.0269	20.7186	0.0082	0.0158
12H	4	115.5	106.455	27.2372	0.0849	38.0940	0.0279	0.0195
12H	5	65.5	107.455	27.6256	0.0201	7.1918	0.0074	0.0201
12H	6	45.5	108.755	28.2495	0.0408	16.1042	0.0083	0.0248
12H	6	145.5	109.755	28.6892	0.0364	12.9878	0.0116	0.0260
13H	1	76.5	111.265	29.3307	0.0220	9.1140	0.0100	0.0214
13H	2	25.5	112.255	29.7069	0.0252	10.9914	0.0103	0.0215
13H	2	125.5	113.255	30.1801	0.0260	12.7722	0.0086	0.0208
13H	3	76.5	114.265	30.8788	0.0143	5.3424	0.0028	0.0233
13H	4	25.5	115.255	31.2915	0.0088	3.9984	0.0019	0.0240
13H	4	75.5	115.755	31.5000	0.0478	10.1920	0.0110	0.0246
13H	4	125.5	116.255	31.7085	0.0176	6.1579	0.0043	0.0197
13H	5	75.5	117.255	32.1254	0.0071	2.6502	0.0019	0.0162
13H	6	75.5	118.755	32.7508	0.0084	4.6158	0.0026	0.0146
13H	6	125.5	119.255	32.9592	0.0088	4.8195	0.0028	0.0130
14H	1	50.5	120.605	33.5214	0.0080	2.6600	0.0028	0.0167
14H	2	1.5	121.615	33.7948	0.0069	2.1868	0.0028	0.0172
14H	2	100.5	122.605	34.0629	0.0124	2.6222	0.0058	0.0228
14H	3	50.5	123.605	34.3337	0.0093	1.6954	0.0049	0.0250
14H	4	0.5	124.605	34.6252	0.0075	2.7160	0.0040	0.0175
14H	4	51.5	125.115	34.7772	0.0116	4.2672	0.0062	0.0200
14H	4	100.5	125.605	34.9234	0.0127	3.5966	0.0068	0.0196
14H	4	101.5	125.615	34.9263	0.0153	3.7674	0.0081	0.0195
14H	5	0.5	126.105	35.0725	0.0067	1.7976	0.0035	0.0203
14H	5	1.5	126.115	35.0755	0.0101	1.6590	0.0053	0.0264
14H	5	50.5	126.605	35.2216	0.0143	2.2372	0.0075	0.0264
14H	5	100.5	127.105	35.3707	0.0272	7.3052	0.0142	0.0230

14H	5	102.5	127.125	35.3767	0.0267	4.8356	0.0139	0.0261
14H	6	0.5	127.605	35.5198	0.0229	6.7018	0.0119	0.0231
14H	6	0.5	127.605	35.5198	0.0371	4.6158	0.0192	0.0354
14H	6	51.5	128.115	35.6719	0.0312	6.2874	0.0161	0.0309
14H	6	75.5	128.355	35.7435	0.0439	8.6520	0.0225	0.0197
14H	6	100.5	128.605	35.8180	0.0631	8.2376	0.0323	0.0250
14H	6	101.5	128.615	35.8210	0.0138	2.5676	0.0070	0.0276
14H	6	125.5	128.855	35.8926	0.0183	2.3114	0.0093	0.0212
14H	7	0.5	129.105	35.9671	0.0395	6.1110	0.0201	0.0300
14H	7	0.5	129.105	35.9671	0.0228	3.3236	0.0115	0.0243
14H	7	19.5	129.295	36.0238	0.0240	2.4892	0.0121	0.0260
14H	7	37.5	129.475	36.0778	0.0433	6.9090	0.0219	0.0146
15H	1	2.5	129.825	36.1869	0.0073	1.0584	0.0036	0.0236
15H	1	25.5	130.055	36.2586	0.0070	0.8946	0.0034	0.0250
15H	1	50.5	130.305	36.3365	0.0046	1.0178	0.0023	0.0168
15H	1	75.5	130.555	36.4144	0.0078	1.3874	0.0039	0.0210
15H	1	100.5	130.805	36.4924	0.0052	1.2110	0.0026	0.0132
15H	1	125.5	131.055	36.5703	0.0093	1.9026	0.0046	0.0210
15H	2	2.5	131.325	36.6545	0.0081	1.1900	0.0040	0.0228
15H	2	25.5	131.555	36.7262	0.0212	3.8794	0.0106	0.0220
15H	2	50.5	131.805	36.8041	0.0076	1.1886	0.0037	0.0172
15H	2	75.5	132.055	36.8820	0.0071	1.5162	0.0035	0.0160
15H	2	100.5	132.305	36.9599	0.0012	0.7070	0.0006	0.0164
15H	3	2.5	132.825	37.1220	0.0072	1.2250	0.0035	0.0210
15H	4	2.5	134.325	37.5896	0.0056	1.2530	0.0027	0.0208
15H	5	2.5	135.825	38.0475	0.0110	1.6030	0.0055	0.0240

Leg 154
Hole 926 B

Sample Core	Segment	cm	Composite Depth Meters	Model Age (Ma)	3He (fmol/g)	3He/4He (x10-6)	ET3He flux fmol/cm2/kyr	Non-Carbonate Fraction
18H	1	77	179.69	6.21	0.0119	0.297	0.0298	0.27
18H	2	80	181.34	6.30	0.0171	0.291	0.0418	0.37
18H	3	78	182.82	6.38	0.0328	0.573	0.0815	0.36
18H	3	78	182.82	6.38	0.0194	0.363	0.0471	0.37
18H	4	81	184.35	6.46	0.0181	0.326	0.0427	0.35
18H	5	78	185.82	6.54	0.0167	0.381	0.0389	0.27
18H	6	80	187.34	6.67	0.0141	0.386	0.0321	0.23
19H	1	78	190.62	6.79	0.0196	0.533	0.0432	0.27
19H	2	78	192.12	6.90	0.0154	0.433	0.0325	0.33
19H	3	78	193.62	6.99	0.0267	0.543	0.0551	0.41
19H	4	81	195.15	7.09	0.0344	0.454	0.0677	0.51
19H	5	78	196.62	7.22	0.0217	0.617	0.0431	0.36
19H	6	78	198.12	7.34	0.0348	0.805	0.0693	0.35
20H	1	27	200.01	7.44	0.0315	0.570	0.0621	0.45
20H	1	48	200.29	7.45	0.0414	0.909	0.0831	0.37
20H	2	48	202.27	7.56	0.0220	0.683	0.0450	0.28
20H	3	48	204.17	7.66	0.0407	1.091	0.0867	0.38
20H	4	48	205.67	7.75	0.0752	1.537	0.1642	0.41
20H	4	48	205.67	7.75	0.0288	0.634	0.0616	0.41
20H	5	48	207.17	7.84	0.0337	0.867	0.0743	0.34
20H	6	48	208.67	7.91	0.0401	0.871	0.0902	0.26
20H	7	5	209.72	7.95	0.0405	0.745	0.0919	0.23
21H	1	48	210.57	7.99	0.0405	0.869	0.0933	0.36
21H	2	48	211.94	8.05	0.0408	0.591	0.0945	0.31
21H	2	48	211.94	8.05	0.0346	0.515	0.0798	0.31
21H	3	48	213.30	8.11	0.0433	1.007	0.1035	0.17
21H	3	82	213.61	8.12	0.0376	0.809	0.0899	0.21
21H	3	107	213.84	8.13	0.0692	1.533	0.1678	0.19
21H	3	107	213.84	8.13	0.0373	0.841	0.0895	0.28
21H	3	132	214.07	8.14	0.0407	0.861	0.0979	0.19
21H	3	147	214.20	8.15	0.0263	0.724	0.0630	0.15
21H	3	147	214.20	8.15	0.0381	1.026	0.0922	0.15
21H	4	14	214.36	8.15	0.0379	0.897	0.0917	0.17
21H	4	48	214.67	8.17	0.0464	1.259	0.1133	0.15
21H	4	48	214.67	8.17	0.0580	1.485	0.1420	0.16
21H	4	82	215.01	8.18	0.0356	0.736	0.0863	0.21
21H	4	108	215.27	8.19	0.0226	0.420	0.0538	0.23
21H	4	130	215.49	8.20	0.0178	0.279	0.0414	0.34
21H	4	145	215.64	8.21	0.0124	0.259	0.0287	0.21
21H	5	25	215.94	8.22	0.0149	0.316	0.0351	0.20
21H	5	48	216.17	8.23	0.0277	0.706	0.0680	0.37
21H	5	48	216.17	8.23	0.0117	0.287	0.0273	0.18
21H	5	82	216.51	8.24	0.0090	0.154	0.0198	0.25

21H	5	108	216.77	8.25	0.0128	0.269	0.0302	0.21
21H	5	132	217.01	8.26	0.0097	0.263	0.0228	0.16
21H	5	142	217.11	8.26	0.0076	0.140	0.0166	0.21
21H	6	21	217.40	8.28	0.0072	0.140	0.0157	0.21
21H	6	21	217.40	8.28	0.0064	0.144	0.0141	0.20
21H	6	25	217.44	8.28	0.0073	0.143	0.0160	0.20
21H	6	48	217.67	8.29	0.0355	0.591	0.0880	0.27
21H	6	48	217.67	8.29	0.0208	0.332	0.0499	0.27
22H	1	48	219.72	8.42	0.0138	0.263	0.0307	0.24
22H	2	48	221.27	8.52	0.0099	0.204	0.0204	0.19
22H	3	48	222.81	8.62	0.0196	0.402	0.0408	0.19
22H	4	48	224.34	8.73	0.0075	0.249	0.0142	0.22
22H	4	48	224.34	8.73	0.0108	0.192	0.0201	0.22
22H	5	48	225.84	8.82	0.0153	0.276	0.0282	0.22
22H	6	48	227.34	8.93	0.0333	0.777	0.0640	0.20
22H	6	48	227.34	8.93	0.0147	0.312	0.0270	0.19
22H	6	48	227.34	8.93	0.0178	0.385	0.0332	0.19
23H	1	48	230.11	9.12	0.0275	0.452	0.0508	0.23
23H	1	48	230.11	9.12	0.0344	0.598	0.0643	0.23
23H	2	48	232.42	9.27	0.0132	0.253	0.0231	0.23
23H	3	48	234.55	9.42	0.0072	0.242	0.0124	0.14
23H	4	48	236.05	9.52	0.0099	0.174	0.0162	0.23
23H	5	48	237.55	9.63	0.0295	0.475	0.0521	0.27
23H	5	48	237.55	9.63	0.0212	0.333	0.0366	0.25
24H	1	75	241.85	9.90	0.0129	0.220	0.0249	0.22
24H	2	74	243.76	10.02	0.0066	0.081	0.0098	0.29
24H	3	74	245.26	10.13	0.0156	0.267	0.0269	0.26
24H	4	74	246.76	10.26	0.0088	0.171	0.0136	0.23
24H	5	74	248.26	10.40	0.0089	0.155	0.0136	0.24
24H	6	74	249.76	10.50	0.0188	0.438	0.0333	0.22

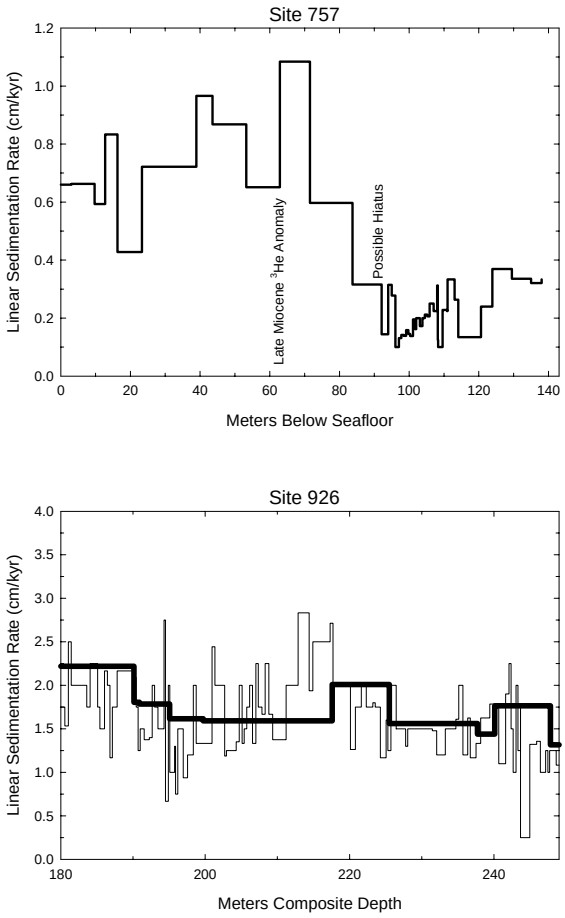

Figure S1. *Linear sedimentation rate models for the two studied ODP holes. In the upper panel (Site 757) the depths of the Late Miocene ^{3}He anomaly and a possible hiatus[7] are indicated. In the lower panel (Site 926) both the orbital-tuning derived sedimentation model (fine line) and the biostratigraphic model (bold line) are shown.*

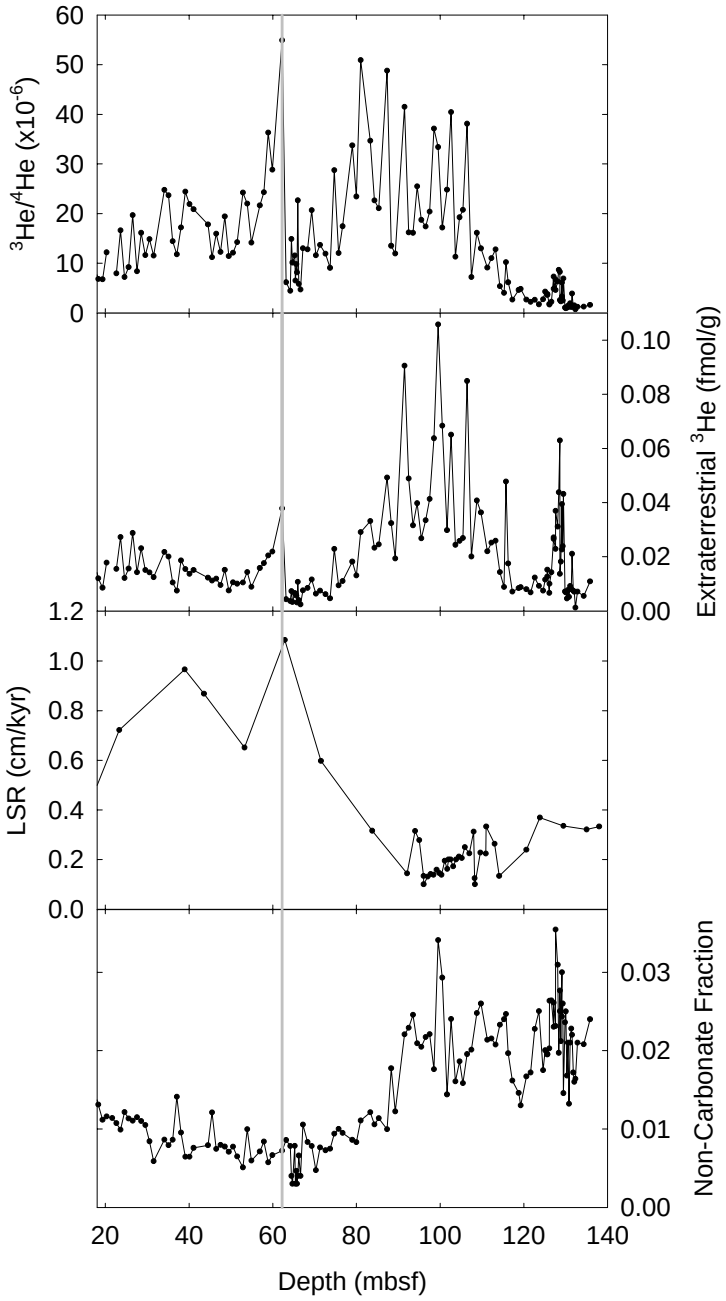

Figure S2. *Detailed comparison of $^3He/^4He$ ratio, extraterrestrial ^3He concentration, linear sedimentation rate (LSR) and non-carbonate fraction (residue after carbonate dissolution with 10% acetic acid) at Site 757. Vertical gray line indicates the onset of the late Miocene ^3He anomaly.*

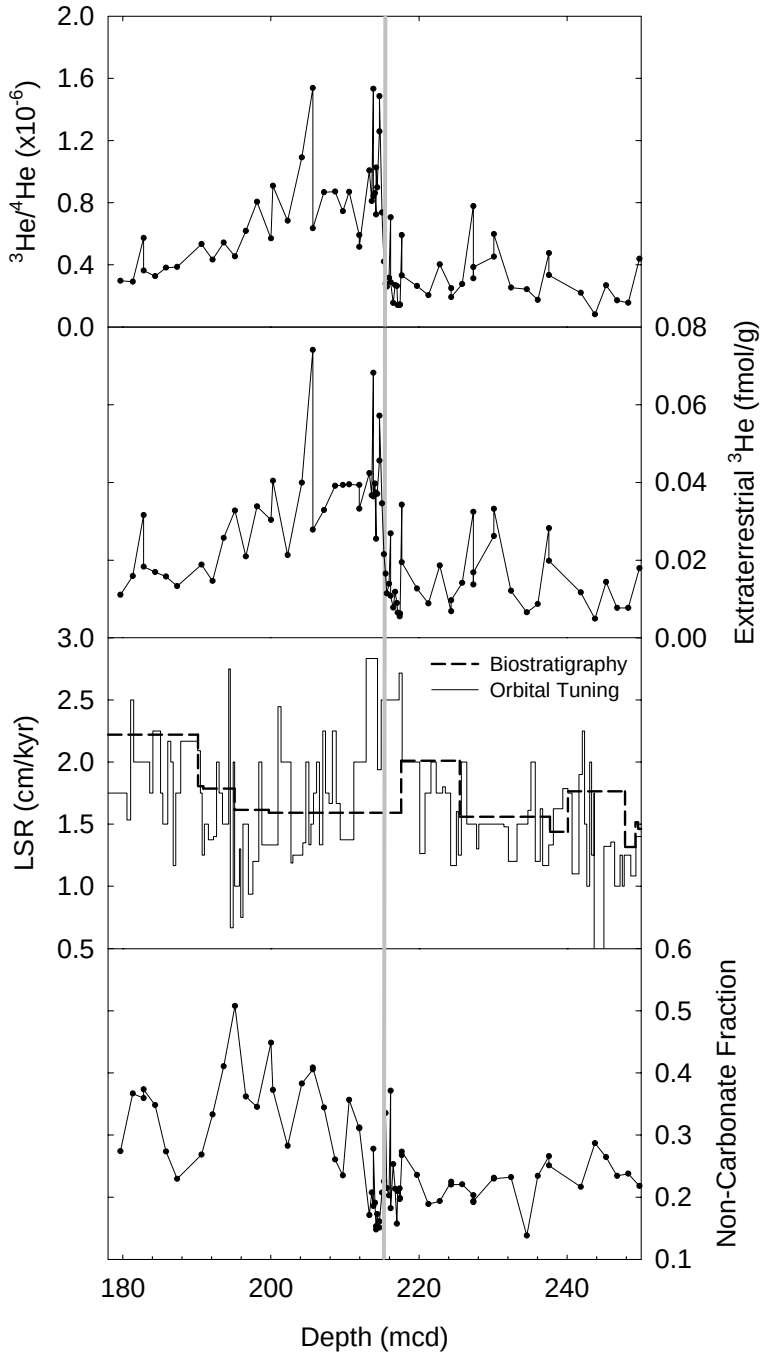

Figure S3. *Detailed comparison of $^3He/^4He$ ratio, extraterrestrial ^3He concentration, linear sedimentation rate (LSR) and non-carbonate fraction at Site 926. The similarity in ^3He and $^3He/^4He$ ratio and the lack of significant changes in sedimentation rate and non-carbonate fraction well-correlated with ^3He indicate a change in extraterrestrial ^3He flux, as discussed previously[3]. Vertical gray line indicates the onset of the late Miocene ^3He anomaly.*

Monte Carlo Dust Evolution Model

Small particles from the Veritas family were assumed to reach Earth through P-R and solar wind drags. We defined the production rate of first-generation Veritas particles as $P(D,t)$, where D is diameter and t is the elapsed time since the family formed. Motivated by results from main belt collisional evolution models[9], we assumed $P(D,t)$ has a segmented cumulative power-law size frequency distribution with index α_1 in the interval (D_{min},D_{break}) and α_2 in the interval (D_{break},D_{max}). We assumed that collisional and dynamical evolution causes $P(D,t)$ to vary such that D_{break}, the diameter at which the power-law slope changes, increases with time according to:

$$\log_{10}\left(\frac{D_{break}}{D_{\min}}\right) = \log_{10}\left(\frac{D_{\max}}{D_{\min}}\right)\left[1 - \exp(-t / \tau_{decay})\right]$$

with D_{min} = 10 μm, D_{max}=1 cm, and τ_{decay} a characteristic decay constant that is described below. The rate of IDP disruptions is defined by the collisional lifetime, $\tau_{col}(D,R)$ that was set to be a function of diameter D and heliocentric distance R (ref 10).

The particles were started at heliocentric distance 3.17 AU. Their orbital evolution were then tracked using P-R and solar drag equations[11] over time t with a timestep Δt = 1000 years. Each surviving particle was followed from heliocentric distance R_t to $R_{t+\Delta t}$ (both in AU) using:

$$R_{t+\Delta t}^{\,2} - R_t^2 = 2.5 \times 10^{-3}\, \beta\, \Delta t$$

$$\beta = 1.15 / (\rho\, D)$$

where the density of the particle is ρ = 1.5 g cm^{-3} and D in microns. Each particle was followed until it disrupted (see below) or reached 1 AU.

At each timestep, we checked to see if the particle was disrupted. The probability of this event was $\Delta t / \tau_{col}(D,R)$. When a particle was found to disrupt, we replaced it with a swarm of fragments that follow a power-law size distribution. We assumed that for each breakup event, the mass of the largest fragment was half that of the parent particle. The power law index of the fragment size distribution is then set by mass conservation[12]. Thus, in our simulations, we follow several generations of particles produced by a collisional cascade; typical runs track the histories of 10^8-10^9 particles.

Using our model, we ran a number of trial cases to determine a reasonable range of input parameters. Our full production runs then used α_1=-2, -2.25, -2.5 and α_2 values between -3 and -4. The former values are shallower than the canonical value of -2.5 (ref 13) because P-R drag quickly removes small particles from the main belt, while the latter values are steeper because we need to link our size distribution to the observed members of the Veritas family while also conserving mass. We also tested values of τ_{decay} = 0.5, 0.75, and 1 Myr, where the timescales were drawn from collision code experiments[9].

We found that the initial breakup of the Veritas family likely produced an IDP population that dominated the main belt population by at least an order of magnitude for ~1 Myr. This would explain both the shape and the decay time of the ^{3}He peak. Our best fit comes from $\alpha_1 = -2.5$, $\alpha_2 = -3.3$ and $\tau_{decay} = 1$ Myr (Figure 2 in main text). It is important to note, however, that the parameters α_2 and τ_{decay} are correlated, with a longer τ_{decay} timescale producing the same solution as a steeper α_2. Our results allow us to rule out (i) steep α_2 values and $\tau_{decay} < 0.5$ Myr values that produce shorter ^{3}He peaks than those observed and (ii) shallow α_2 and $\tau_{decay} > 1.5$ Myr values that create longer ^{3}He peaks than those observed.

Late Miocene vs. Late Eocene Event

Given the success of our model in matching the Veritas breakup to the Late Miocene ^{3}He event and the similarity in the ^{3}He patterns at ~35 and ~8.2 Myr ago, it is possible that an asteroid collision also produced the Late Eocene peak (Figure 1 in main text). However, we find no evidence for the disruption of an asteroid larger than ~100 km diameter in the main belt other than Veritas over the last ~100 Myr (ref 14). Moreover, because the Late Eocene event must also produce a short-lived but prominent asteroid shower to account for the two large craters, candidate families must inject numerous bodies into a resonant "escape hatch" that can quickly and with high efficiency move this material onto Earth-crossing orbits. It is unclear whether any recently-formed families are consistent with this criterion. For this reason, the Late Eocene event remains a mystery.

Other Putative Features in the ^{3}He Sediment Record

At least one other recent asteroid breakup event has a known age over the sampled interval shown in Figure 1 (main text), namely that of the Karin cluster. The Karin cluster was produced 5.75 ± 0.05 Myr ago from the disruption of a $D = 33$ km asteroid in the Koronis family[15,16]. This event, while far smaller than the Veritas breakup, has produced a dust band observed by infrared telescopes. In Figure 1 (main text), we find a moderate increase in the ^{3}He flux near that time, but no pronounced spike like that of the Late Miocene or Eocene events. We cannot yet say whether this increase is associated with the Karin breakup or is merely representative of the background flux from that epoch. A comprehensive study of this issue is left for future work.

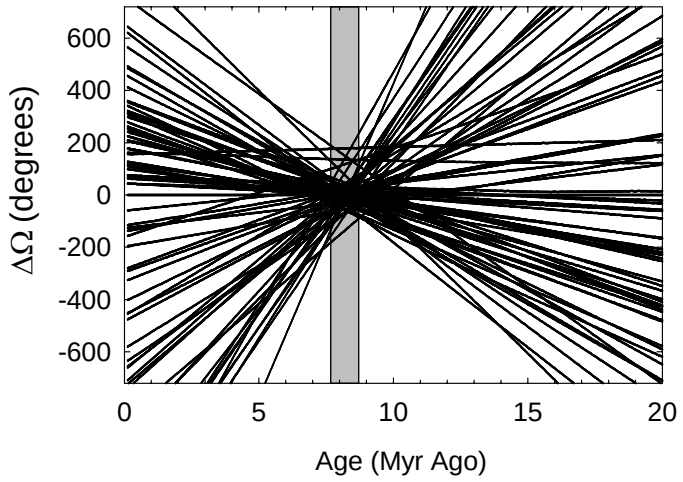

Figure S4. *Convergence of nodal longitudes suggests that the Veritas family formed by a catastrophic collision at 8.3 ± 0.5 Myr ago (see also ref 14 for an alternative way to plot the same data), gray band. Immediately after the disruption, the fragments all circled the Sun, as a group, in nearly identical orbits. Over time planetary perturbations forced their orbital orientations (specified by the longitude of the ascending node and argument of perihelion) to drift away from each other, eventually spreading out uniformly. By numerically integrating the present orbits of large asteroid members of the Veritas family back in time, we discovered a clustering of nodal longitudes. The figure shows orbital histories of nodal longitudes relative to that of large member asteroid (1086) Nata (ΔΩ). The mean ΔΩ is ~40^{o} at t ~ 8.3 Myr, much smaller than at other times, suggesting a strong statistical significance of the nodal alignment.*

References

1. Peirce, J., Weissel, J. et al., Proceedings of the Ocean Drilling Program, Initial Reports, Leg 121 (Ocean Drilling Program, College Station, 1991).
2. Curry, W. B., Shackleton, N. J., Richter, C. et al., Proceedings of the Ocean Drilling Program, Initial Reports, Leg 154 (Ocean Drilling Program, College Station, 1995).
3. Patterson, D. B. & Farley, K. A. Extraterrestrial 3He in seafloor sediments: evidence for correlated 100 kyr periodicity in the accretion rate of interplanetary dust, orbital parameters, and Quaternary climate. Geochimica et Cosmochimica Acta 62, 3669-3682 (1998).
4. Farley, K. A., Love, S. G. & Patterson, D. B. Atmospheric entry heating and helium retentivity of interplanetary dust particles. Geochimica et Cosmochimica Acta 61, 2309-2316 (1997).
5. Backman, J. & Raffi, I. Calibration of Miocene nannofossil events to orbitally tuned cyclostratigraphies from Ceara Rise, in Proceedings of the Ocean Drilling Program, Scientific Results, vol 154 (eds. Shackleton, N. J., Curry, W. B., Richter, C. & Bralower, T. J.) 83-99 (Ocean Drilling Program, College Station, 1997).
7. Martin, E. E. & Scher, H. D. Preservation of seawater Sr and Nd isotopes in fossil fish teeth: bad news and good news. Earth and Planetary Science Letters 220, 25-39 (2004).
8. Shackleton, N. J. & Crowhurst, S. Sediment fluxes based on an orbitally tuned time scale 5 Ma to 14 Ma, Site 926, in Proceedings of the Ocean Drilling Program, Scientific Results, vol 154 (eds. Shackleton, N. J., Curry, W. B., Richter, C. & Bralower, T. J.) (Ocean Drilling Program, College Station, 1997)
9. Bottke, W. F. et al. The fossilized size distribution of the main asteroid belt. Icarus 175, 111-140 (2005).
10. Grun, E., Zook, H. A., Fechtig, H. & Giese, R. H. Collisional balance of the meteoritic complex. Icarus 62, 244-272 (1985)
11. Burns, J. A., Lamy, P. L. & Soter, S. Radiation forces on small particles in the Solar-System. Icarus 40, 1-48 (1979).
12. Nolan, M. C. & Greenberg, R. Stochastic-evolution of asteroids to produce the ordinary chondrites. Meteoritics 24, 310-310 (1989).

13. Dohnanyi, J. S. Collisional model of asteroids and their debris. Journal of Geophysical Research 74, 2531-2554 (1969).
14. Nesvorný, D., Bottke, W. F., Levison, H. F. & Dones, L. Recent origin of the solar system dust bands. Astrophysical Journal 591, 486-497 (2003).
15. Nesvorný, D., Bottke, W. F., Levison, H. F. & Dones, L. A recent asteroid breakup in the main belt. Nature 417, 720-722 (2002).
16. Nesvorný, D., & Bottke, W. F. Detection of the Yarkovsky effect for main belt asteroids. Icarus 170, 324-342 (2004).